



RESEARCH ARTICLE

10.1029/2019JG005216

Soil Fluid Biogeochemical Response to Climatic Events

Yaniv Olshansky¹ , John F. Knowles^{2,3} , Greg A. Barron-Gafford^{2,4} , Craig Rasmussen¹ , Nate Abramson⁴, and Jon Chorover¹

Key Points:

- Impacts of ecosystem processes on soil geochemical reactions were measured in real time using a set of instrumented pedons
- The soil CO₂ response to infiltration events depended on ecosystem productivity, position, initial soil moisture conditions, and seasonality
- Data showed periods of prevalent CO₂ dissolution in water and consumption in weathering reactions, which resulted in pulses of solutes

Supporting Information:

- Supporting Information S1

Correspondence to:

J. Chorover,
chorover@email.arizona.edu

Citation:

Olshansky, Y., Knowles, J. F., Barron-Gafford, G. A., Rasmussen, C., Abramson, N., & Chorover, J. (2019). Soil fluid biogeochemical response to climatic events. *Journal of Geophysical Research: Biogeosciences*, 124, 2866–2882. <https://doi.org/10.1029/2019JG005216>

Received 19 APR 2019

Accepted 26 JUL 2019

Accepted article online 23 AUG 2019

Published online 9 SEP 2019

Corrected 22 OCT 2019

This article was corrected on 22 OCT 2019. See the end of the full text for details.

¹Department of Soil, Water and Environmental Science, University of Arizona, Tucson, AZ, USA, ²School of Geography and Development, University of Arizona, Tucson, AZ, USA, ³Southwest Watershed Research Center, USDA-ARS, Tucson, AZ, USA, ⁴Biosphere 2, University of Arizona, Tucson, AZ, USA

Abstract Predicting fluid biogeochemistry in the vadose zone is difficult because of time-dependent variation in multiple controlling factors, such as temperature, moisture, and biological activity.

Furthermore, soils are multicomponent, heterogeneous porous media where manifold reactions may be affecting solution chemistry. We postulated that ecosystem-scale processes, such as carbon fixation and ecohydrologic partitioning, control subsurface biogeochemical reactions, including mineral weathering. To test this hypothesis, we applied a novel “instrumented pedon” research approach. Analysis of the data streams demonstrates the interactions between pulsed wetting events and biogeochemical processes in the soil profile, and along groundwater flow paths. Rapid wetting front propagation into dry soil resulted in a pulsed increase in CO₂ partial pressure in deeper soil layers, whereas wetting front propagation into a premoistened soil profile showed the opposite effect. The apparent respiratory quotient (ARQ), calculated from CO₂ and O₂ fluxes, deviated from expected oxidative ratios particularly during soil wetting events. These deviations were correlated in time with pore water geochemical responses, revealing that a fraction of the respired CO₂ was consumed locally in pulsed silicate weathering events that accompanied wetting-front propagation. However, most of this CO₂ was dissolved in the soil pore water and transported downgradient, and along the soil-bedrock interface, where a portion of it was further consumed in silicate weathering reactions, and another portion was degassed to the atmosphere. These results highlight the tight coupling that exists between physical, biological, and chemical processes, on event time scales, during incremental co-evolution of the critical zone, particularly in water-limited systems.

Plain Language Summary Prediction of the flow of elements in soil is challenging due to the complex and varied nature of the belowground environment. This study aimed to resolve the influence of weather events, such as melting snow or rainfall during different seasons, on biological and chemical reactions in the soil. In a mountain headwater environment, we measured physical and chemical factors in multiple locations and depths, beginning above ground and extending to the depth of bedrock. Our data demonstrate that rapid wetting of a dry soil resulted in a pulsed increase of carbon dioxide concentration, more than half of which was not emitted from the soil. Some of this carbon dioxide was consumed by chemical weathering reactions that release rock-derived elements to the soil solution. A large fraction of this respiratory carbon dioxide was dissolved in the soil water and transferred to deeper soil layers, groundwater, and streams. This information contributes to a better understanding of the seasonal links between vegetation growth, mineral weathering, and soil carbon dioxide emissions to the atmosphere.

1. Introduction

Nutrient cycling in the critical zone (CZ) is controlled by hydrobiogeochemical processes in soil and regolith. Such processes include microbial fixation of atmospheric nitrogen, dissolution of macronutrients and micronutrients (e.g., P, Ca, Mg, K, Fe, Zn, and Mn), and organic matter partitioning and decomposition (Perdrial et al., 2015). Meteoric inputs of radiant energy, water, and gases, particularly gaseous CO₂ and O₂, are primary drivers of these processes, and over long time scales, they affect the co-evolution of soil and ecosystems (Rasmussen et al., 2011). Accretion, respiration, and decomposition of plant and microbial biomass infuses inorganic C and soluble organic matter into the bio-active weathering zone (Taylor et al., 2009). This labile carbon fuels microbial respiration when water is also available, resulting in fluctuations in gas partial pressures, and in the composition and speciation of soil solution, which in turn are buffered by rapid adsorption-desorption and slower mineral transformation reactions (Brantley & Olsen, 2013;

©2019. The Authors.

This is an open access article under the terms of the Creative Commons Attribution License, which permits use, distribution and reproduction in any medium, provided the original work is properly cited.

Perdrial et al., 2015; Taylor et al., 2009). During periods of prolonged wetting (which limits gas-phase diffusion) and heterotrophic microbial activity, soils can become depleted in O_2 , leading to transitions in redox status and the microbial use of alternative terminal electron acceptors (e.g., NO_3^- , Mn^{IV} , and Fe^{III}) in respiration and associated (im)mobilization of such elements in soils (Fiedler et al., 2007). Although it is well known that such interacting biotic and abiotic processes occur in field soils, their concurrent measurement in situ, particularly in response to pulsed episodes of carbon and water infusion, remains a significant challenge to soil science.

Numerous prior studies have documented the effects of variation in soil solution chemistry on ion exchange, organic matter partitioning, and mineral weathering reactions in a wide range of soils (e.g., Brantley & Olsen, 2013; Chorover & Amistadi, 2001; Sposito, 1984). However, these studies have largely been conducted in laboratory experiments, wherein a specific set of aqueous geochemical conditions are imposed, and the kinetic or equilibrium response of the soil system is measured. While crucial to enabling an improved understanding of soil chemical processes, such studies do not capture the dynamic and variable response in soil solution chemistry that likely results from the pulsed nature of meteoric inputs (e.g., fluctuating wet-dry cycles), which is particularly important in water-limited regions with wet and dry seasonality. Conversely, there are numerous published studies of variation in soil solution chemistry measured in the field as a function time or season, depth or landscape position (e.g., Chadwick & Chorover, 2001; Chorover et al., 1994; McIntosh et al., 2017; Vázquez-Ortega et al., 2015). However, very few (Andrews & Schlesinger, 2001; Oh et al., 2007) have been informed by co-located measurements of physical and biogeochemical parameters that drive this variation, such as wetting front propagation or biologically imposed gas phase (CO_2 or O_2) fluctuations. Without such complementary datasets, it is difficult to develop a mechanistic interpretation of controls over soil solution chemistry that can be incorporated into reactive transport models to enable better prediction of CZ evolution (Li et al., 2017).

In the semiarid southwestern United States, ecosystem productivity and associated soil weathering processes are limited to periods of time when temperature and moisture are concurrently suitable for biological activity and chemical reactions. Water limitation to heterotrophic microbial activity in such systems, for example, is evident from numerous observations of pulsed CO_2 evolution resulting from soil wetting following prolonged dry periods (Placella et al., 2012; Xiang et al., 2008). Several competing hypotheses exist for this observation, including that wetting leads to desorption of labile organic matter into soil pores, making it available for rapid microbial degradation (Zhang et al., 2014). Uncertainty as to the underlying mechanism of this “Birch Effect” (Birch, 1958) is due, in part, to the fact that no prior studies have sought to measure in situ dissolved organic carbon (DOC) concentrations in field soils undergoing moisture-induced elevation of partial pressure of CO_2 (P_{CO_2}). Irrespective of cause, we postulate that the associated increase in P_{CO_2} (and possibly DOC) associated with wetting front propagation will perturb the soil system, inducing a shift in pH and solution chemistry, promoting ion exchange, and weathering of soil minerals. This effect implies that chemical denudation of the CZ in water-limited systems occurs in pulsed responses to meteoric inputs of water that, in turn, drive microbial activity. Recent studies (Angert et al., 2015; Sánchez-Cañete et al., 2018) suggest that a significant portion of CO_2 produced by heterotrophic respiration in the subsurface is not emitted directly to the atmosphere and is therefore available to drive biologically enhanced weathering reactions. Based on continuous measurements of soil CO_2 efflux and O_2 influx, the ARQ may be calculated to evaluate the amount of CO_2 that has been produced by heterotrophic respiration. Sánchez-Cañete et al. (2018) suggested that more than half of the CO_2 produced in heterotrophic soil respiration may be dissolved in soil solution, thereafter contributing to mineral dissolution, while being transported vertically or laterally to groundwater and streams.

We hypothesized that pulsed biological activity resulting from periodic meteoric inputs and their impacts on ensuing biogeochemical reactions would be resolvable with a novel “instrumented pedon” research approach. The approach co-locates soil moisture, soil temperature, soil CO_2 and O_2 , and soil oxidation reduction potential sensors with pore water samplers as a function of depth in distinct landscape positions. While the sensors provide continuous data streams, the samplers enable episodic sampling to assess soil solution response to sensor parameters. We postulated that pulsed episodes of CO_2 and moisture would result in solution chemistry changes that reflect ion exchange and weathering reactions. We tested for these relations in a montane field setting in the Santa Catalina Critical Zone Observatory (Tucson, AZ, USA),

which is subjected to a bimodal precipitation regime (summer monsoon and winter rain/snowmelt). Specifically, we expected that solution chemistry would fluctuate in response to biological activity that is driven by temporal and spatial variation in soil moisture and temperature.

2. Materials and Methods

2.1. Site Description and Experimental Design

The study site is a small (0.016 km²) zero-order basin (ZOB) located on the west side of Mt. Bigelow (elevation: 2,532–2,574 m) within the Santa Catalina Mountains Critical Zone Observatory (Figure 1). The climate is subhumid, with a mean annual temperature of 9.4°C and a mean annual precipitation of 609 mm. The precipitation regime is bimodal and is mainly delivered as winter snow or rainfall (November–April) or summer monsoon rainfall (July–September) separated by a dry early summer season (May–June). During winter, ephemeral snow cover may accumulate and ablate several times. Ponderosa pine (*Pinus ponderosa*) and Douglas-fir (*Pseudotsuga menziesii*) dominate the site with a mean canopy height of 10 m. A relatively shallow soil (approximately 1 m) is underlain by Paleozoic aged metamorphic rocks of schist and quartzite (Joseph, 1968). A geophysical survey of the ZOB suggested strong north-south aspect contrast, with a shallower weathering profile occurring on north facing relative to south facing aspects (<5 and >10 m, respectively) resulting from bedrock foliation differences (Leone et al., 2016).

2.2. Field Data Collection

This study aimed to probe linkages between above and belowground processes that control subsurface geochemical reactions. Therefore, a combination of data sets deriving from micrometeorology, instrumented pedons, and a surface water flume at the ZOB outlet were used, as described below.

Evapotranspiration (ET) and the net ecosystem exchange of CO₂ (NEE) were determined using the eddy covariance technique. In this way, each turbulent flux was calculated as the mean covariance between deviations in vertical wind speed and mixing ratio sampled at 10 Hz by a sonic anemometer (CSAT 3, Campbell Scientific, USA) and infrared gas analyzer (Li-7500, Li-Cor, USA) co-located at 29.8 m above ground level on a tower immediately adjacent to the ZOB (Figure 1; Brown-Mitic et al., 2007; Chang et al., 2018). The 10-Hz data were subsequently averaged to 30-min mean values and filtered for periods of insufficient turbulent mixing; two-dimensional coordinate rotation and standard corrections for density fluctuations and sensor heating were also applied (Burba et al., 2008; Lee et al., 2004). Gross primary production (GPP) was derived from the NEE flux by extrapolating nighttime respiration throughout the day (Reichstein et al., 2005). Missing data were gap-filled with the average value under similar meteorological conditions (Falge et al., 2001; Reichstein et al., 2005).

Four pedons were excavated and instrumented in the ZOB in November 2014. The intent was to provide representation of upper and lower locations in the convergent zone (i.e., the central axis of the catchment), as well as north facing and south facing planar hillslopes (Figure 1). The north and south facing planar sites provided strong contrast in weathering profile depth and also snow ablation dynamics (with south facing slopes normally ablating faster than north facing slopes). The upper and lower convergent sites were selected to represent hydrologic mixing zones with progressively larger upgradient catchment contributing areas, farthest from and closest to the ZOB outlet, respectively. The volumetric contribution of large rock fragments was estimated visually in the field (Schoeneberger et al., 2012), and gravel was quantified during sieving. Soil samples collected as a function of depth during pedon excavation were air-dried, sieved to recover the <2-mm fraction, mixed for homogeneity, and stored at room temperature prior to analysis.

Pedons were equipped at multiple depths with sensors for continuous monitoring of temperature and volumetric water content (5TM, Decagon, Pullman, WA, USA), O₂ molar fraction (SO-110, Apogee, Logan, UT, USA), and CO₂ molar fraction (GMM222 and GMM221, Vaisala, Houston, TX, USA). These sensors were co-located with soil solution samplers (2- μ m pore size; Prenart SuperQuartz, Prenart Equipment ApS, Frederiksberg, Denmark) at 10-, 30-, and 60-cm depth and at the soil-bedrock interface (varying from 60 to 115 cm depending on pedon). Redox potential was measured using Pt probes connected to Ag|AgCl reference electrodes (Paleo Terra, Amsterdam, The Netherlands) installed at 10, 30, and 60 cm. All probes were connected to dataloggers (CR1000, Campbell scientific, Logan, UT, USA), which collected measurements every 30 s and stored 30-min averages. When available, soil water samples were collected

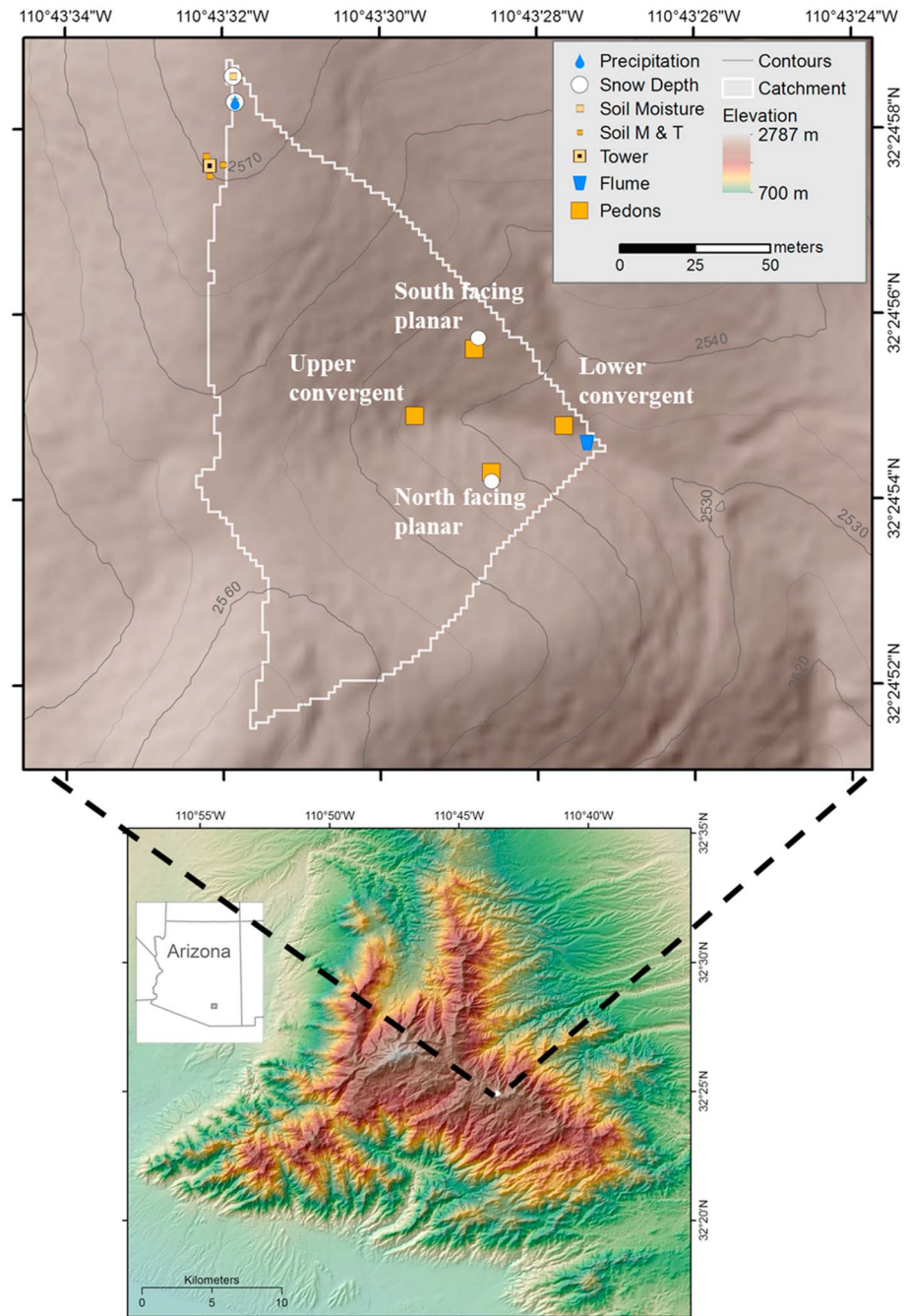


Figure 1. Digital elevation map of the Bigelow zero order basin derived from bare earth light detection and ranging data, showing locations of instrumented pedons (orange squares) and other instrumentation.

from each Prenart sampler into acid-washed high density polyethylene (HDPE) bottles by applying a vacuum of 40 kPa.

The ephemeral outlet of the ZOB was instrumented with a Parshall flume fitted with a pressure transducer (InSitu Level TROLL 500 15 psig Model: 89010) that measured stage height. Due to low and infrequent flow, meaningful discharge data were not collected, but stream water samples were collected for chemical analysis from the flume into acid-washed 1 L polypropylene bottles, manually or using an automatic water sampler (Teledyne ISCO, Lincoln, NE, USA).

2.3. Aqueous Sample Preparation

Chemical analysis of the collected samples was performed in the University of Arizona Laboratory for Emerging Contaminants (ALEC). All water samples were packed on ice and filtered within 48 hr of collection using 0.45- μm nylon filters. Sample aliquots for dissolved inorganic and organic carbon (DIC and DOC, respectively) were filtered through combusted 0.7- μm glass-fiber filters.

2.4. Solution Phase Analysis

Sample aliquots for major and minor solutes (Na^+ , Mg^{2+} , K^+ , Ca^{2+} , Al, Si, Mn, Fe, Sr, and Zr) were preserved in acid-washed HDPE bottles by acidification to approximately pH 2 using trace metal grade nitric acid. All water samples were stored at 4°C prior to analysis by inductively coupled plasma mass spectrometry (Perkin Elmer ELAN DRC II inductively coupled plasma mass spectrometry, Shelton, CT prior to 2013 and thereafter Agilent 7700x) equipped with either a dynamic reaction (Perkin Elmer) or collision (Agilent) cell to eliminate molecular mass interferences. DIC and DOC were measured using a Shimadzu TOC-VCSH analyzer (Shimadzu Scientific Instruments, Columbia, MD). Major anions (Cl^- , NO_3^- , SO_4^{2-} , and PO_4^{3-}) were measured by ion chromatography (Dionex ICS-1000 equipped with an AS22 Analytical Column, Sunnyvale, CA, USA).

2.5. Solid Phase Analysis

Collected soils were air dried, sieved to isolate the <2-mm fraction and prepared for physical, chemical, and mineralogical analyses. Soil pH was measured on all samples at mass to volume ratios of 1:1 (soil:water). Particle size distribution was determined by laser diffraction using a Beckman Coulter LS 13 320 laser diffraction particle size analyzer following pretreatment with NaOCl adjusted to pH 9.5 to remove organic matter and dispersion with 48 h mixing on a rotary shaker with 5% sodium hexametaphosphate. For quantitative X-ray diffraction (XRD), samples were run as random powder mounts following treatment to remove organic matter and mixing with an internal corundum reference, measured from 5 to 65° 2 θ , with a step size of 0.02° 2 θ , using a PANalytical X'Pert PRO-MPD X-ray diffraction system (PANalytical, Almelo, AA, the Netherlands). The resulting diffractograms were analyzed using a combination of Rietveld analyses (Moore & Reynolds, 1997) and the RockJock program (Eberl, 2003) to identify primary mineral phases and mineral abundance following methods outlined in Lybrand and Rasmussen (2018).

2.6. Data processing and statistical analysis

Data processing and statistical analyses were performed using R (Akima & Gebhardt, 2016; Fox & Weisberg, 2011; Lenth, 2015; Pinheiro et al., 2017; R Core Team, 2017; Wickham, 2009). The ratio between CO_2 efflux and O_2 influx (ARQ), was calculated as

$$\text{ARQ} = -0.76 \frac{\Delta c}{\Delta o} \quad (1)$$

where -0.76 is the ratio of CO_2 and O_2 diffusion coefficients and Δc and Δo are the differences in mole fraction for gases in the atmosphere and at soil depth (Angert et al., 2015; Sánchez-Cañete et al., 2018).

Since soil pore water samples were collected using suction (section 2.2), and due to the large difference between soil and atmospheric P_{CO_2} , a significant amount of dissolved CO_2 may be degassed from the sample upon collection. This process may alter both DIC and pH values. Therefore, both pH and DIC were calculated using P_{CO_2} and temperature measured in the soil profile (section 2.2), and alkalinity of the collected sample calculated as

$$[\text{Alk}] = [\text{Na}^+] + [\text{K}^+] + 2[\text{Ca}^{2+}] + 2[\text{Mg}^{2+}] - [\text{Cl}^-] - 2[\text{SO}_4^{2-}] - [\text{NO}_3^-] \quad (2)$$

(Stumm & Morgan, 1996).

Visual Minteq 3.1 was used for geochemical speciation modeling. Mixed effect model and analysis of variance (ANOVA) techniques were used to assess differences in soil variables between sampling dates and locations, and Tukey's honest significant difference test used to assess difference between means, using lme, Anova, and lsmeans functions in R (Fox & Weisberg, 2011; Lenth, 2015; Pinheiro et al., 2017).

3. Results

3.1. Soil Properties

Soil depth varied from 60 to 80 cm in the convergent zones, and soils were classified as fine-loamy, mixed, superactive, mesic Typic Argiudolls. Soils of the north and south planar landscape positions were slightly deeper (100 to 115 cm, respectively) and classified as fine, mixed, superactive, mesic Typic Argiudolls. All profiles contained an argillic horizon, superimposed with a cobbly colluvial layer of varying thickness (approximately 10 to 40 cm; Table 1). Clay content increased with depth from 10 to 20% in the top horizon to up to 50% in the bottom horizon overlying partially weathered bedrock. Soils exhibited slight to moderate acidity (pH range from 4.8 to 6.3; Table 1).

Quantitative XRD results (Figure 2) demonstrate similar mineral composition in the four profiles. The primary mineral assemblage was dominated by quartz (40 to 55%) followed by mica (14%), orthoclase (7%), plagioclase (6%), and small amounts of clinoptilolite and amphiboles (approximately 2% each). Secondary minerals included illite (11%), kaolinite (5%), vermiculite and smectite (approximately 3% each), and iron oxides (<1%).

3.2. Meteoric Driver Dynamics

Annual rainfall depth varied over the 3 years of the study, totaling 720, 630, and 420 mm during monitoring years 2015, 2016, and 2017 (Figure 3). Most of the rain (70 to 90%) fell during summer and fall (May to November each year). While 2017 had the overall lowest precipitation, the wettest month during the study was July 2017, with a total precipitation of 270 mm, which was double the amount of the second wettest month (August 2016). Ephemeral snow cover occurred between December to March each year, with the highest snow depth measured in winter 2016 (50 cm) followed by 2017 (45 cm) and 2015 (30 cm). Volumetric soil water content (θ) closely tracked the precipitation pattern ($p < 0.001$, repeated measures ANOVA), with decreasing annual means from 2015 to 2017 of 0.21 (0.001), 0.19 (0.001), and 0.17 (0.001), respectively (standard deviations in parentheses). Also, θ was significantly higher during the exceptional high precipitation event of July 2017. The mean θ for July 2017 was 0.20 (0.004) relative to values of 0.14 (0.003) and 0.17 (0.003) for 2016 and 2015, respectively. During the wet seasons, formation of an intermittent perched water table was observed at the soil-bedrock interface in the north facing planar and lower convergent pedons (Figure 3).

GPP and ET followed a seasonal pattern with increased values during the warm season (Figure 3). In 2015, GPP increased steadily from January to July, then declined during fall and winter. Interestingly, during the drier years of 2016 and 2017 a decrease in GPP was observed in June and July, before increasing again in August (Figures 3 and S1). This trend was more pronounced in 2017, the driest year. The mean daily GPP in 2017 was slightly higher than in 2016 (4.16 ± 1.76 , and 3.69 ± 1.54 g C · m⁻² · day⁻¹, respectively, $p < 0.001$, repeated measures ANOVA [Tukey]), and was similar to 2015 (3.93 ± 1.76 , $p = 0.21$). The most significant difference in daily GPP for 2017 compared with 2016 and 2015 was observed in August (6.4 ± 0.21 , 4.8 ± 0.21 , and 5.1 ± 0.21 g C · m⁻² · day⁻¹, respectively, $p < 0.001$). It is important to note that the high GPP value during August 2017 followed the large rainfall of July 2017. The ET followed a similar annual trend to GPP; however, differences between the three years were less pronounced.

The soil temperature ranged from 0 to 23°C (Figure 3) and was highest during June to August ($15.2 \pm 1.8^\circ\text{C}$) and lowest during January ($3.5 \pm 1.2^\circ\text{C}$). The overall soil P_{CO_2} pattern followed the annual air temperature trends, with higher values during the summer and lower values during the winter (Figure 3). Within each soil profile, the lowest P_{CO_2} was measured in the top soil (repeated measures ANOVA [Tukey], $p < 0.001$), whereas the highest concentrations fluctuated between the deeper and middle layers depending on specific location and time (Figure 3).

Although pulsed wetting events resulted in rapid changes in P_{CO_2} , the direction of the change was dependent on location and time. In the south facing planar and upper convergent landscape locations, rapid increases in soil P_{CO_2} were observed as a response to increases in θ throughout the study period (Figure 3). Conversely, the north facing planar and lower convergent locations exhibited more complex θ - P_{CO_2} relations (Figures 3 and 4). Specifically, under relatively dry conditions (i.e., $\theta < 0.2$), pulsed increases in P_{CO_2} occurred in response to increases in θ . However, when the infiltration pulse occurred under relatively wet initial conditions (i.e., $\theta > 0.2$), P_{CO_2} decreased rapidly. Hence, the hysteresis relations between θ and

Table 1
Soil Physicochemical Characteristics

Sample ID	Horizon	Depth	Clay	Silt	Sand	Rock fragment	pH	Organic matter
Upper convergent	Oi	0–2	20.3	52.5	27.2	30	5.29	31.41
		2–5	21.9	48.4	29.7	30	5.04	12.38
		5–10	22.0	45.0	33.1	30	5.73	12.75
		10–20	26.6	45.1	28.4	30	5.68	10.38
	A2	20–30	38.4	39.8	21.9	25	5.72	7.59
	A3	30–40	32.8	39.1	28.2	25	4.93	5.86
	Bt	40–62	35.8	34.1	30.2	5	4.92	5.53
North facing planar	A1	0–2	20.5	49.5	30.0	40	5.48	23.80
		2–5	20.4	53.3	26.4	40	5.70	28.63
	A2	5–10	22.4	54.5	23.2	40	5.75	23.58
		10–20	24.7	43.9	31.5	20	5.89	9.15
		20–30	26.6	44.3	29.1	20	5.34	6.53
	Bt1	30–40	34.1	34.7	31.2	20	5.19	5.42
		40–60	39.2	24.4	36.5	20	5.07	5.78
		60–80	48.0	23.6	28.4	10	5.16	6.42
	Bt2	80–90	46.8	24.2	29.1	10	5.28	5.83
South facing planar	O	0–2	11.6	36.7	51.8	40	5.44	64.18
	A1	2–5	17.7	53.3	29.1	40	5.66	51.22
		5–10	18.0	55.5	26.5	40	5.45	10.63
		10–20	18.3	51.3	30.4	40	5.65	7.49
		20–30	18.6	53.4	28.0	10	5.41	6.00
	A2	30–40	17.0	52.0	31.0	15	5.19	3.83
		A4	40–60	14.7	38.5	46.9	15	4.88
	Bt1	60–80	25.7	45.3	29.1	20	4.82	4.49
	Bt2	80–100	44.6	39.0	16.5	10	5.40	5.24
	Bt3	100–115	49.8	35.2	15.0	5	5.36	5.22
	Lower convergent	Oa	0–2	15.9	50.8	33.4	20	6.16
Oi		2–5	18.7	49.8	31.6	20	6.29	10.23
A1		5–10	18.4	45.0	36.6	30	5.92	7.36
A2		10–20	20.4	45.8	33.8	30	5.86	5.66
A3		20–30	24.4	46.5	29.2	25	4.99	5.33
		30–40	28.1	42.2	29.8	25	5.94	5.61
Bt1		40–60	26.7	30.6	42.7	20	5.63	4.43
Bt2		60–80	32.9	23.4	43.7	20	4.90	4.90

P_{CO_2} were soil moisture dependent at these pedons. Clockwise hysteresis was observed during relatively dry conditions and anticlockwise hysteresis under relatively wet conditions (Figure 4). It is important to note that the large depletion in P_{CO_2} from the soil profiles coincided with the existence of the perched water table. However, the perched water table occurred at the soil-bedrock interface, while significant CO_2 depletion was observed above this layer (Figure 3). Soil P_{O_2} concentrations remained close to atmospheric during much of the study period, with periodic excursions to low levels observed during periods of high θ conditions, particularly lower in the profile near the soil-bedrock interface (Figure 3).

3.3. Soil Solution Chemistry

Soil solution chemistry data are presented for the four pedons in Table 2. Mean pH was slightly acidic, ranging from 5.4 to 6.5, and Ca^{2+} and HCO_3^- were the dominant ions in solution. The upper layer of each pedon contained higher K^+ , Al, Fe, HCO_3^- , Mg^{2+} , and DOC concentrations relative to the lower part of the profile

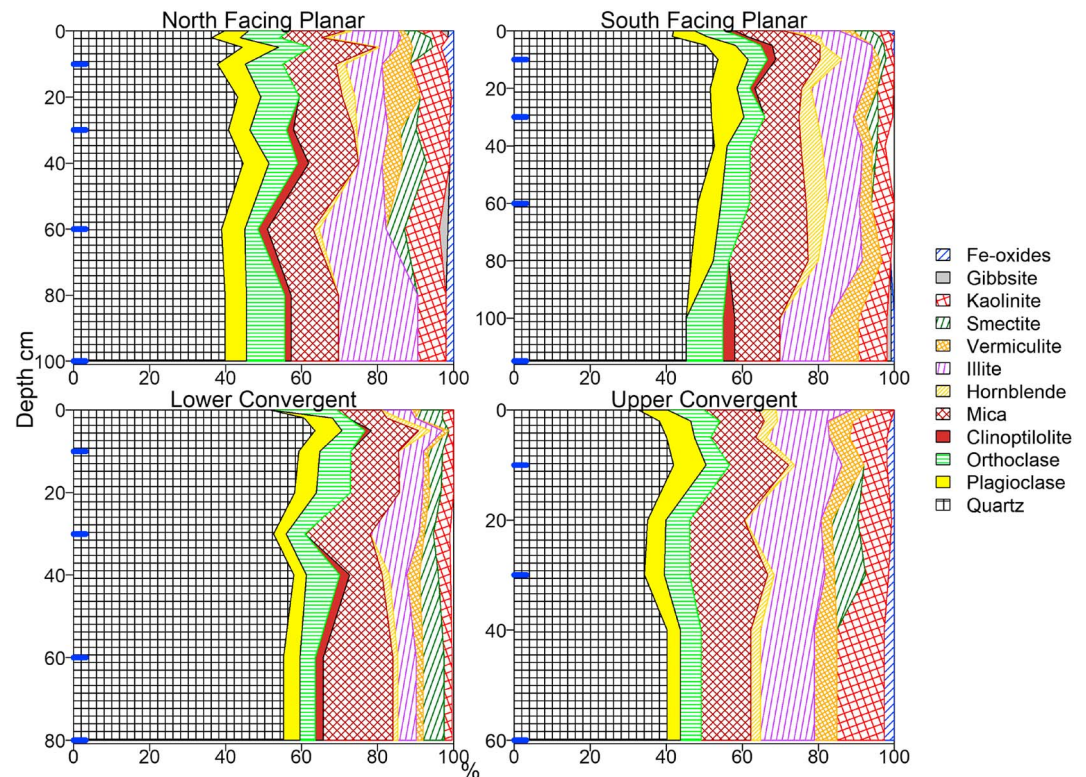


Figure 2. Mineral distribution with depth at the four pedons. The blue ticks show the depth of sensor/sampler installations.

(repeated measure ANOVA [Tukey], $p < 0.01$), whereas Na^+ and SO_4^{2-} showed the opposite trend (repeated measure ANOVA [Tukey], $p < 0.01$). Other elements did not show consistent trends with depth.

Although solute concentrations were highly variable in time and space, only minor differences were observed in mineral stabilities and saturation indices (Figure 5). Mineral stability diagrams indicate that kaolinite formation controls Si concentration in the soil solution. Soil pore waters were undersaturated with respect to the dominant primary minerals and saturated with respect to the secondary phases observed in the soil profile (Figures 2 and 5). All water samples were undersaturated with respect to calcite.

Time series analysis of rock-derived solutes, exemplified here for the north facing pedon (60 cm depth), show high time-variability in concentration (Figure 6; coefficients of variance range from 40 to 90%). During the summer monsoon, mean concentrations of nonhydrolysing cations, strong acid anions, and Si were 61.94 ± 3.18 , 54.73 ± 3.50 , and 36.97 ± 2.27 $\text{mmol}/\text{m}^3_{\text{soil}}$, respectively. These values were significantly higher than during the winter and dry seasons (repeated measure ANOVA [Tukey], $p < 0.01$). Al concentrations were similar between the summer and winter (1.14 ± 0.07 , and 1.22 ± 0.09 $\text{mmol}/\text{m}^3_{\text{soil}}$, respectively), but significantly higher than dry periods (0.72 ± 0.13 $\text{mmol}/\text{m}^3_{\text{soil}}$, repeated measure ANOVA [Tukey], $p < 0.01$). Although Fe showed the highest concentration variability (i.e., coefficients of variance = 90%), it did not show a clear seasonal pattern. The highest solute concentrations were measured during mid-August to early September 2017, approximately 1 month after the large rain event (July 2017; Figures 3, 6, and 7). During this period, Si concentrations increased from approximately 30 to 60 and 80 $\text{mmol}/\text{m}^3_{\text{soil}}$ (Figure 7). Si concentration peaks followed peaks in P_{CO_2} with a lag of 7 to 25 days.

To test for relations between P_{CO_2} and Si concentration, a cross-correlation analysis was performed for each pedon and depth independently (Figure S2). Results indicate a significant positive correlation between the two variables for 13 out of 16 locations. The highest correlation between P_{CO_2} values and soil solution Si was observed for a lag of 2 to 30 days (R^2 ranged from 0.2 to 0.8, $p < 0.05$). In addition, surface water collected during spring snowmelt at the outlet of the ZOB also showed a lag of approximately 14 days between peaks in

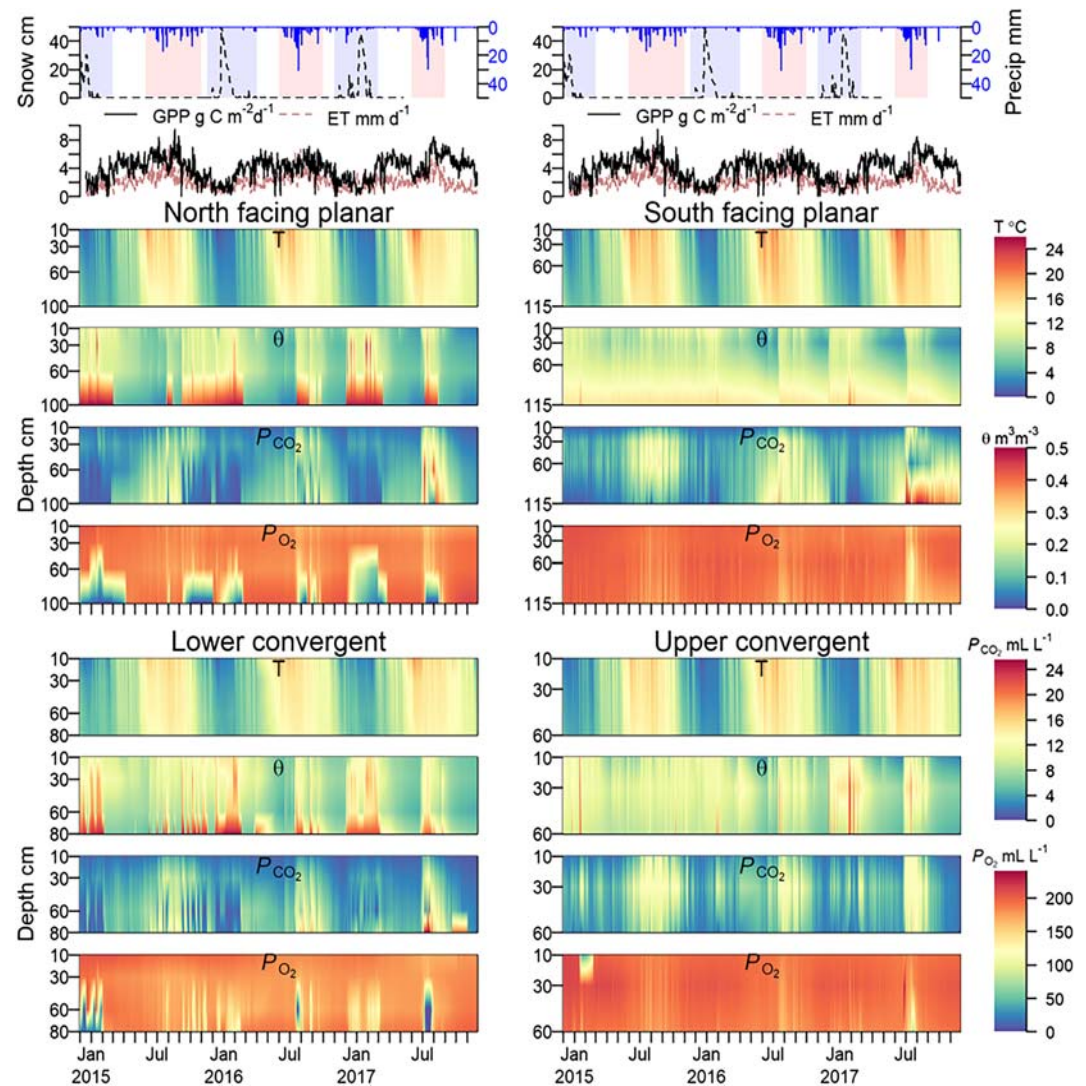


Figure 3. Time series of snow depth (dashed line) and precipitation (solid blue line), gross primary production (solid black line) and evapotranspiration (dashed brown line) measured at the Mt. Bigelow tower (top panels), bivariate interpolation of soil temperature, volumetric water content (θ), P_{CO_2} and P_{O_2} .

P_{CO_2} and Si concentration (Figure 8). Similar lags between peak P_{CO_2} and Ca^{2+} and Na^+ were also observed in both stream and soil pore water, although these relations were less pronounced than the Si trend.

4. Discussion

4.1. Water and Gas Dynamics

Time series data obtained from flux tower and instrumented pedon measurements (Figures 3 and 4) indicate two distinct mechanisms that control the relations between soil water content and gas phase CO_2 concentration. The first occurred with increased soil water content following a relatively dry period that resulted in a rapid heterotrophic respiration pulse and increased CO_2 concentration (i.e., the “Birch Effect”; Birch, 1958). During the warm season, the magnitude of these pulses was larger than in the cold season, and longer dry periods were followed by larger respiration pulses. This trend was most pronounced during 2017 when a long dry season preceded the summer monsoon (Figure 3). These results corroborate previous studies demonstrating significant C losses from subsurface soils following rewetting of soils after prolonged drought (Barron-Gafford et al., 2011; Smith et al., 2017). In contrast to the pulsed increase in CO_2 concentration after

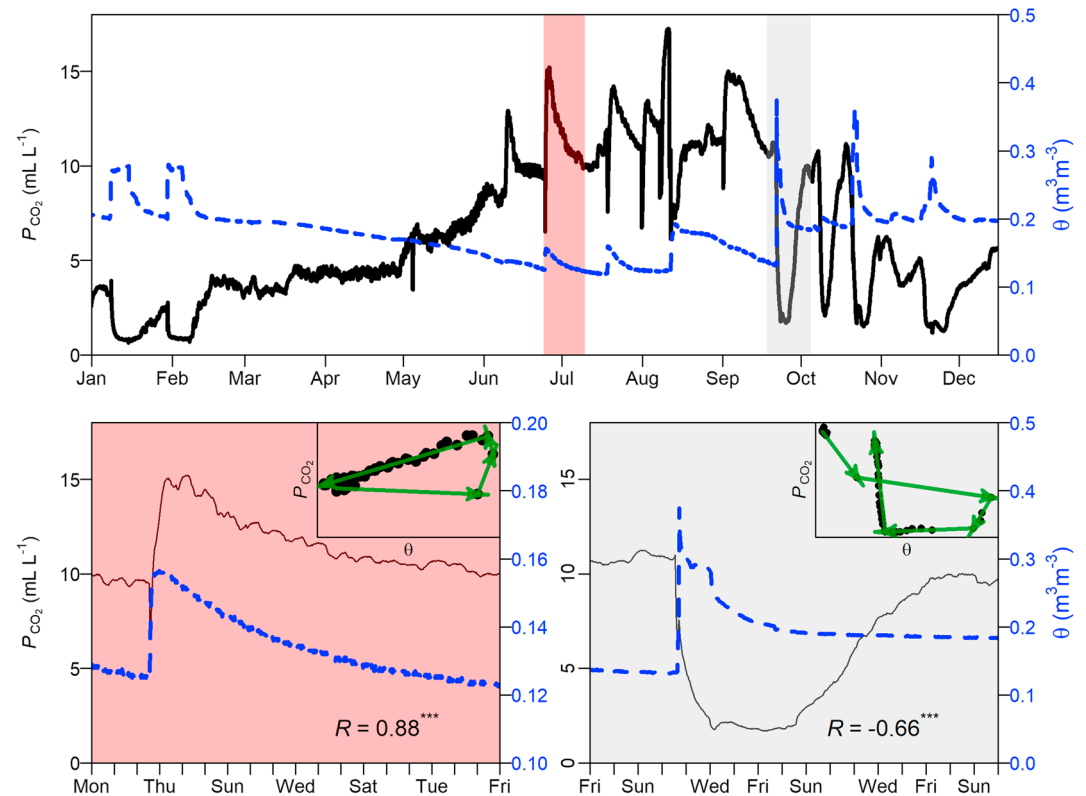
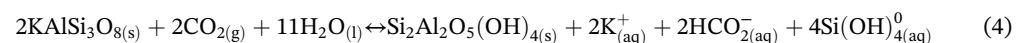
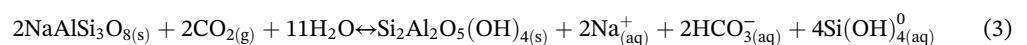


Figure 4. Time series of P_{CO_2} (solid black line) and θ (dashed blue line), recorded during 2015 at the north facing planar pedon depth 60 cm (top panel). Shaded areas are expanded in the bottom panel and represent wetting events during the monsoon (red) and fall (grey). Pearson correlations and significance are indicated in each of the expanded plots. Insets in the expanded plot demonstrates hysteresis between CO_2 and θ .

rewetting of dry soils, an infiltration flux to previously moist soils resulted in rapid depletion of gas phase CO_2 in the soil subsurface. This depletion can be attributed to dissolution of CO_2 in soil pore water. We observed this second type of relation between CO_2 and soil water content at the instrumented pedons in the north facing planar and lower convergent sites. In these pedons, establishment of an intermittent perched water table disconnected gas filled pores at depth from the upper soil layers, diminishing the gaseous diffusion of CO_2 out of and O_2 into the soil, and limiting heterotrophic production of CO_2 . Limited CO_2 diffusion subsequently promoted larger CO_2 mass transfer from gas to solution phase. The south facing planar and upper convergent pedons did not exhibit the same pattern of CO_2 depletion during infiltration to moist soil, nor formation of a perched water table. These results are consistent with more deeply weathered bedrock on the south facing slope, as observed in a prior geophysical survey of the Bigelow ZOB (Leone et al., 2016), allowing faster drainage of the soil at the bedrock interface.

4.2. The Soil and Stream Chemistry Response to P_{CO_2} Dynamics

Time series analyses of soil pore water and stream solutions, and soil P_{CO_2} (section 3.2), demonstrate a lag of several days to 4 weeks between peak CO_2 and Si concentrations (Figures 7, 8, and S2). Soil mineral assemblage (Figure 2), stability diagrams, and soil solution saturation indices (Figure 5) indicate dominance of plagioclase and orthoclase weathering to kaolinite. The relevant incongruent dissolution reactions for these minerals are



On the basis of the lag between peak CO_2 and Si, we can estimate the reaction rate:

Table 2
Summary of pH and Solute Chemistry for Soil Solution Collected From Bigelow ZOB Instrumented Pedons

Pedon	Depth	pH	Si	Fe	Al
Upper convergent	10	5.8 (0.68)	208 (108)	2.3 (0.56)	5.7 (1.38)
	30	5.4 (0.50)	178 (54)	2.5 (1.16)	4.0 (1.92)
	60	5.9 (0.61)	172 (61)	6.2 (4.35)	9.6 (6.26)
North facing planar	10	6.5 (0.23)	160 (75)	6.8 (4.20)	13 (6.3)
	30	6.1 (0.27)	156 (51)	8.0 (4.42)	15 (4.0)
	60	5.6 (0.59)	152 (79)	1.9 (1.77)	5.0 (1.67)
South facing planar	100	5.9 (0.59)	127 (64)	1.0 (1.59)	1.4 (1.68)
	10	6.5 (0.35)	189 (101)	11 (8.6)	21 (15)
	30	6.1 (0.17)	147 (47)	4.9 (1.95)	7.7 (2.62)
	60	5.8 (0.47)	220 (93)	0.9 (0.64)	1.5 (1.12)
Lower convergent	115	6.3 (0.62)	161 (69)	0.6 (1.46)	0.4 (0.55)
	10	6.5 (0.21)	127 (28)	6.1 (1.18)	15 (2.4)
	30	5.6 (0.91)	117 (42)	3.5 (3.88)	6.3 (2.83)
	60	5.8 (0.94)	146 (41)	1.0 (2.02)	0.9 (1.68)
80	6.1 (0.40)	181 (69)	0.5 (0.46)	0.6 (0.68)	
Pedon	Depth	Na ⁺	Mg ²⁺	K ⁺	Ca ²⁺
Upper convergent	10	36 (14)	49 (10)	119 (73)	122 (42)
	30	80 (13)	56 (13)	47 (8)	102 (31)
	60	85 (28)	55 (20)	35 (10)	91 (30)
North facing planar	10	33 (15)	82 (88)	145 (75)	186 (75)
	30	57 (10)	52 (10)	48 (9)	96 (18)
	60	55 (19)	42 (10)	13 (34)	50 (23)
South facing planar	100	59 (42)	39 (10)	9.6 (5.03)	59 (22)
	10	41 (18)	71 (30)	133 (42)	126 (54)
	30	49 (7)	47 (7)	91 (13)	95 (12)
	60	61 (12)	55 (11)	66 (21)	84 (19)
Lower convergent	115	54 (15)	58 (13)	61 (213)	104 (28)
	10	21 (9)	38 (7)	163 (20)	113 (22)
	30	63 (16)	49 (15)	40 (11)	90 (19)
	60	75 (15)	54 (12)	23 (6)	97 (32)
80	110 (114)	65 (12)	32 (8)	128 (53)	
Pedon	Depth	Cl ⁻	SO ₄ ²⁻	NO ₃ ⁻	HCO ₃ ⁻
Upper convergent	10	44 (49)	8.3 (8.79)	79 (51)	253 (159)
	30	145 (129)	34 (5)	131 (131)	90 (68)
	60	94 (33)	27 (5)	68 (91)	153 (127)
North facing planar	10	42 (37)	12 (10)	213 (535)	493 (323)
	30	59 (44)	27 (10)	13 (17)	204 (80)
	60	61 (39)	24 (4)	39 (72)	80 (78)
	100	65 (56)	22 (4)	18 (22)	110 (71)
South facing planar	10	32 (30)	25 (10)	30 (35)	412 (161)
	30	45 (11)	37 (9)	66 (46)	182 (69)
	60	101 (32)	40 (8)	70 (56)	134 (85)
Lower convergent	115	85 (29)	30 (6)	52 (38)	169 (96)
	10	38 (13)	19 (0)	110 (63)	158 (71)
	30	81 (39)	30 (8)	93 (108)	101 (87)
	60	105 (33)	40 (6)	58 (84)	151 (101)
80	124 (23)	54 (36)	63 (40)	169 (73)	

Note. Mean values are in μM ; standard deviations are in parentheses.

$$R = \frac{\Delta C_{si}}{2\rho_s \Delta t S f} \quad (5)$$

where ΔC is difference between max and baseline Si concentration ($\text{mol}/\text{m}^3_{\text{soil}}$), ρ_s is the soil bulk density ($1.5 \text{ g}/\text{m}^3$), Δt is the lag time (s) between Si and P_{CO_2} peaks, S (m^2/g^1) is the specific surface area, and f is the mass fraction of feldspars. The surface area was estimated from the silt and sand portion of the particle size distribution (excluding clay size fraction, which is essentially devoid of feldspar), assuming spherical

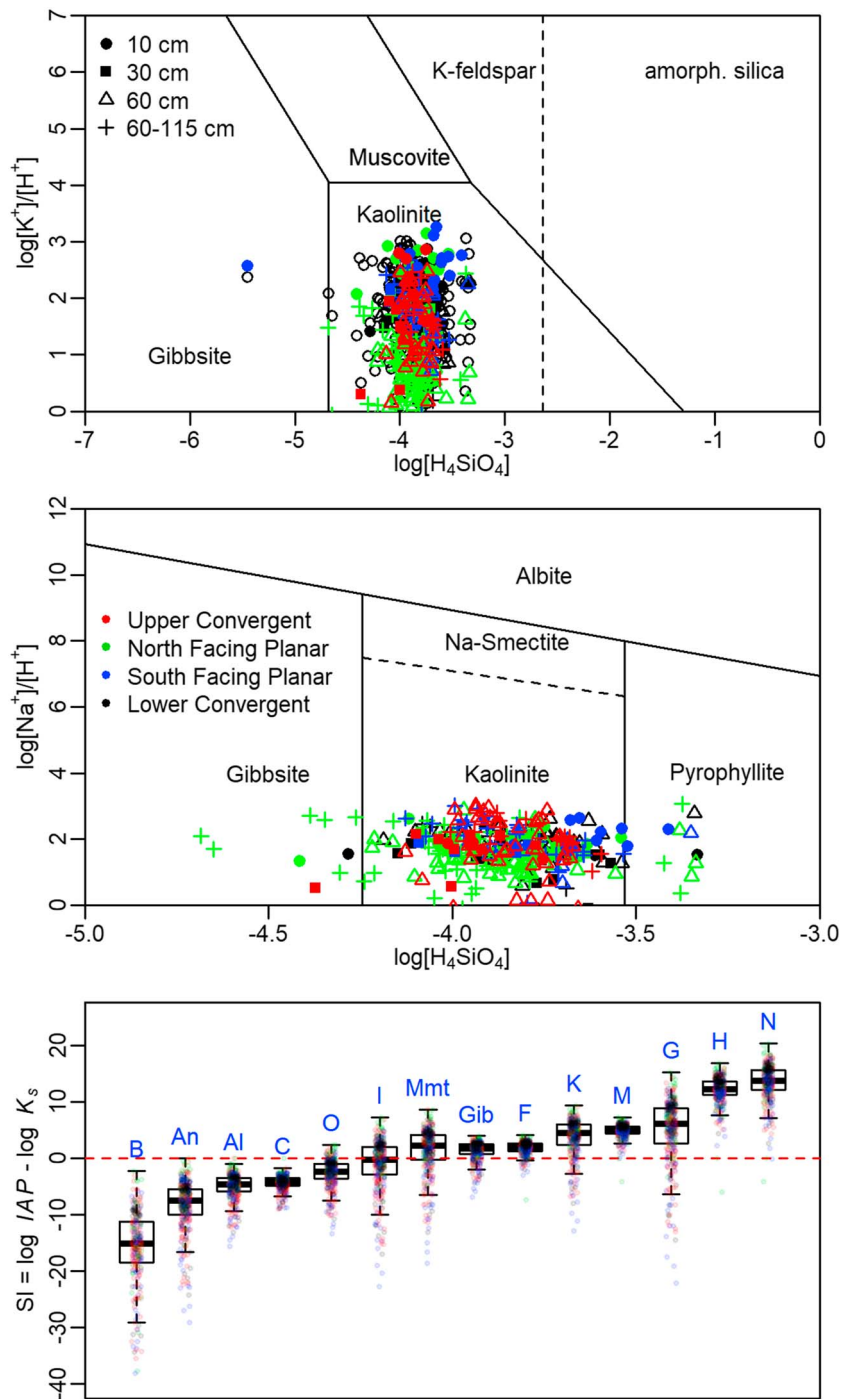


Figure 5. Stability diagrams for selected K (upper panel) and Na (middle panel) phases, and saturation indices calculated for selected mineral phases. B, biotite; An, anorthite; Al, albite; C, calcite; O, orthoclase; I, illite; Mmt, montmorillonite; Gib, gibbsite; F, ferrihydrite; K, kaolinite; M, muscovite; G, goethite; H, hematite; N, nontronite.

particle geometry and particle density of 2.65 g/m^3 . The estimated reaction rate ($\log R$) was between -13.5 and -12.7 , which is within the range of laboratory and field-based reaction rates reported by White and Brantley (2003). Using relations between weathering rates and time from incipient weathering (White & Brantley, 2003), the time from incipient weathering was estimated between 100 to 5,000 years. The fact that most of the mineral weathering reactions occurred during episodic periods, rather than

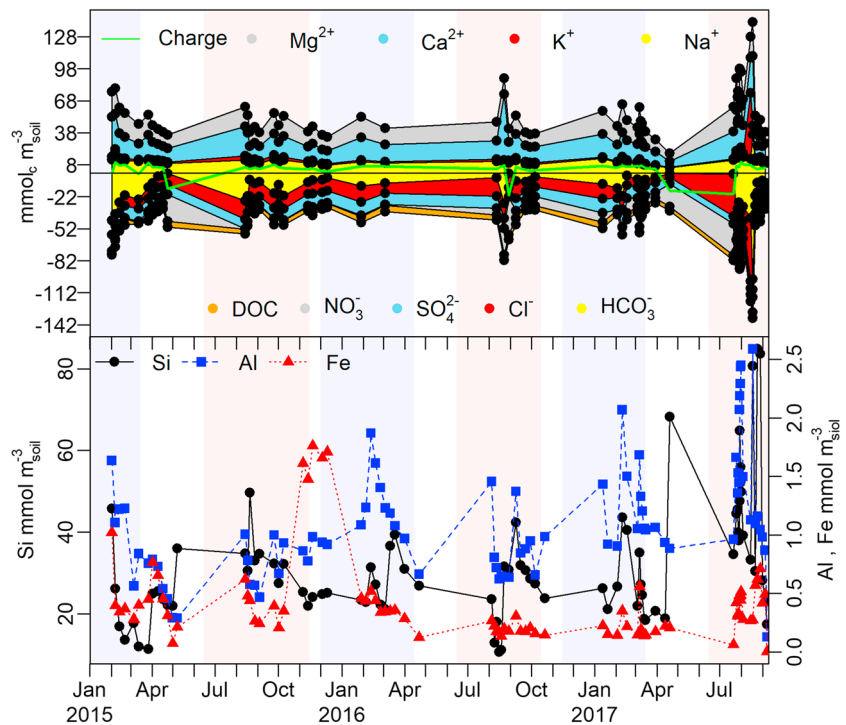


Figure 6. Time series of charge balance between nonhydrolysing cations and strong acid anions (top), and Si, Fe, Al (bottom). Shaded area represents winter rain and snowmelt (blue) and summer and fall rain (red). Data collected from the north facing pedon at depth of 60 cm.

continually, further suggests that the time from incipient weathering was likely on the longer end of that range (White & Brantley, 2003). In comparison, modeled soil residence times for a similar forested catchment in the Santa Catalina Mountains indicated soil residence times range from ~4 to 16 ky (Chang et al., 2018; Pelletier & Rasmussen, 2009) for divergent and convergent landscape positions, respectively.

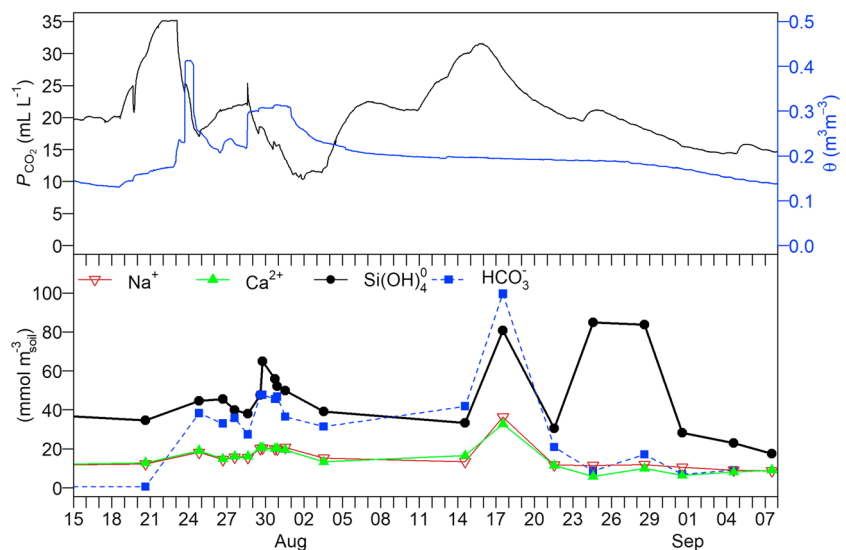


Figure 7. Soil P_{CO_2} , Si concentrations, and volumetric water content during peak P_{CO_2} between July and September 2017 from the north facing pedon 60-cm depth.

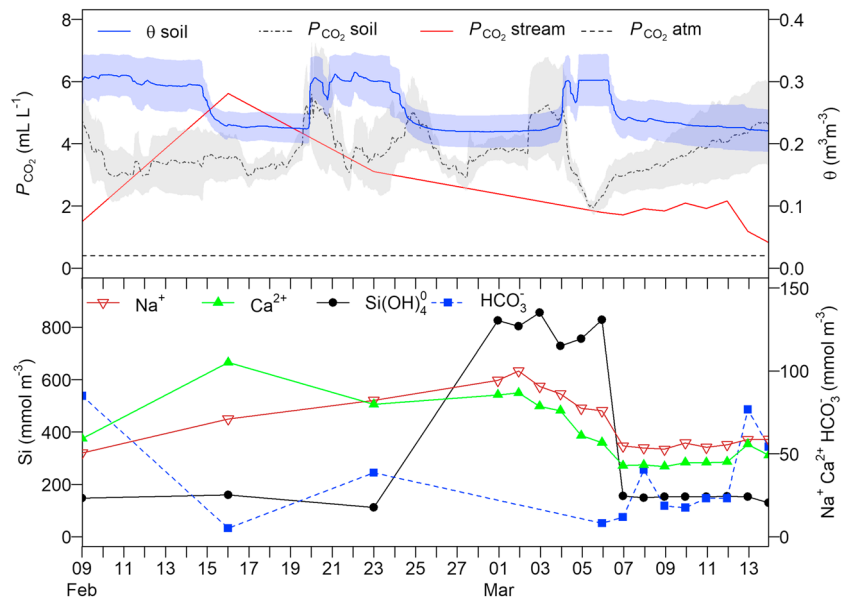


Figure 8. Stream P_{CO_2} and Si concentrations during the 2017 snowmelt period.

4.3. The ARQ and the Fate of “Missing” CO_2

The calculated ARQ (equation (1)) of the north facing pedon at 60-cm depth varied between approximately 0 during periods of high water content (Figures 3, 9, and S2–S4) and 0.52 during drier and warm periods. Given the average oxidative ratio of organic matter, which is calculated based on the moles of O_2 consumed per mole of CO_2 produced during mineralization of natural organic matter (Masiello et al., 2008), an ARQ

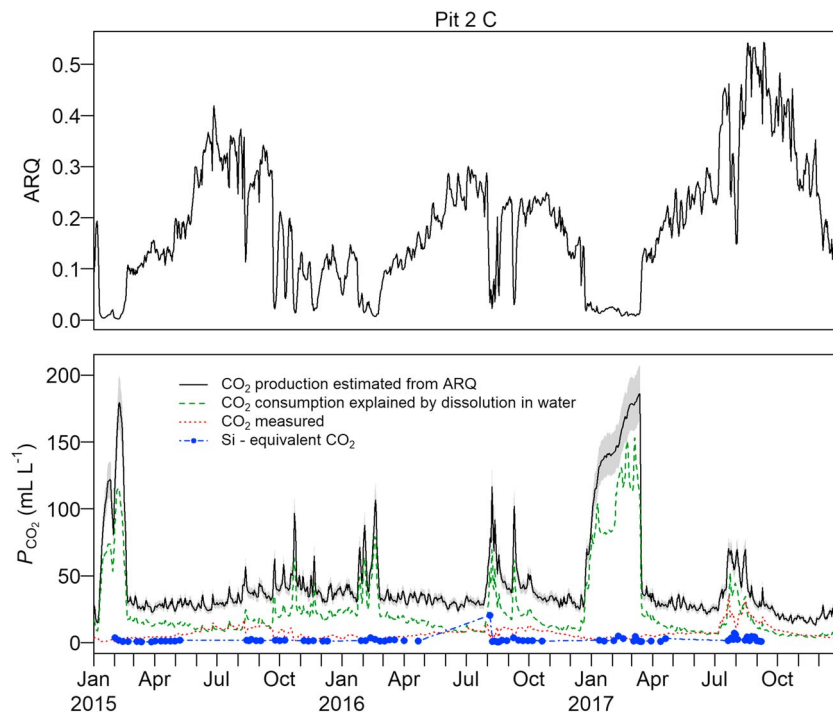


Figure 9. (top) Apparent respiratory quotient (ARQ). (bottom) Apparent P_{CO_2} calculated from ARQ (equation (6); solid line), estimated amount of CO_2 that can be dissolved in water (dashed green line), measured P_{CO_2} (dotted red line), and Si concentration in equivalence of CO_2 (blue dot-dashed line and filled circles). Shaded area represents error in P_{CO_2} calculation. Data obtained from north facing planar at 60 cm.

value of 0.9 ± 0.1 is consistent with expectations if all CO_2 produced in the subsoil is vertically effluxed from the soil surface. In our case, ARQ values were consistently <0.9 (Figures 9 and S2–S4). Assuming that the oxidative ratio of organic matter is indeed 1.1 (Masiello et al., 2008), the total moles of CO_2 produced by respiration in the soil ($P_{\text{CO}_2\text{-ARQ}}$) were derived from the ratio between the optimal (0.9 ± 0.1) and measured ARQ:

$$\frac{P_{\text{CO}_2\text{-atm}} - P_{\text{CO}_2\text{-ARQ}}}{\Delta c} = \frac{0.9}{\text{ARQ}} \quad (6)$$

where $P_{\text{CO}_2\text{-ARQ}}$ is the atmospheric P_{CO_2} (approximately 0.4 ml/L), ARQ is calculated using equation (1), and Δc is the difference in CO_2 mole fraction between gas concentration in the atmosphere and at soil depth. Results indicate that the measured P_{CO_2} was lower than $P_{\text{CO}_2\text{-ARQ}}$ by a factor of 1 to 200. The highest deviation between the two P_{CO_2} values occurred during periods of high soil water content (Figure 3).

In prior work, CO_2 dissolution in water and CO_2 consumption by mineral weathering reactions were suggested as mechanisms that may explain the differences between measured and calculated P_{CO_2} (Angert et al., 2015; Sánchez-Cañete et al., 2018). Since water entering the soil profile can be assumed to be in equilibrium with atmospheric P_{CO_2} , the maximum amount of CO_2 that can be subsequently dissolved in these meteoric low CO_2 pore waters can be calculated based on reequilibration with the high $P_{\text{CO}_2\text{-ARQ}}$ of the gas filled pores. Results of this calculation demonstrate that $60 \pm 14\%$ of the difference between measured P_{CO_2} and calculated $P_{\text{CO}_2\text{-ARQ}}$ can be explained by dissolution of CO_2 into the aqueous phase (Figures 9 and S3–S5). Further, during periods of relatively high soil water content (i.e., $\theta > 0.2$), CO_2 dissolution explained $71 \pm 11\%$ of the difference between observed and predicted CO_2 concentrations, indicating that this mechanism was dominant during high volumetric water content conditions.

To assess the potential amount of CO_2 consumed by silicate weathering reactions, the Si concentrations were converted to P_{CO_2} equivalence using the ideal gas law, and the stoichiometric ratio of CO_2 and Si for feldspar incongruent dissolution. Results show that only a small fraction of the $P_{\text{CO}_2\text{-ARQ}}$ (approximately 6%) can be explained by mineral weathering consumption (Figures 9 and S3–S5).

The microbial community, its carbon use efficiency, and the presence of autotrophic organisms, were also suggested to affect the ARQ value (Angert et al., 2015; Sánchez-Cañete et al., 2018). Nevertheless, our data show that a large portion of the deviation in ARQ from expected oxidative ratios can be explained by CO_2 dissolution in the soil pore water. Moreover, increases in soil P_{CO_2} , enhanced silicate dissolution reaction rates, and all pore water chemistry indicate that most of the dissolved CO_2 is not consumed locally in silicate weathering reactions (Figures 7 and 9). This dissolved CO_2 is, therefore, transported with the water flux and may be further consumed by mineral weathering reactions along hydrologic flow paths through deeper unconsolidated parent material (Calabrese et al., 2017) or during lateral flow along the soil-bedrock interface en route to the stream. Dissolved CO_2 that is not consumed along the water flow line may degas to the atmosphere as groundwater emerges to the stream, and stream water chemical composition corroborates higher P_{CO_2} of the stream compared with atmospheric P_{CO_2} (Figure 8). However, deeper weathering is also evidenced by the pronounced increase in stream Si concentrations that were observed approximately 14 days after peak in P_{CO_2} (Figure 8) and are consistent with active silicate weathering along soil and groundwater flowlines.

5. Conclusions

In this study, the impacts of ecosystem metabolism on soil geochemical reactions were directly measured by installing instrumented pedons within the footprint of a flux tower. The analysis provided several key points. Firstly, pulsed wetting front propagation following rain or snowmelt resulted in differential subsurface P_{CO_2} responses. At relatively low initial θ (<0.2), a combination of heterotrophic and autotrophic respiration produced a rapid increase in soil P_{CO_2} , whereas at high initial θ (> 0.2), CO_2 that accumulated over time under moist soil conditions was rapidly depleted from the soil profile. The latter process is often overlooked in ecosystem C cycling studies (Cueva et al., 2019) and demonstrates the potential importance of hydrological sweeping and transport of CO_2 . Secondly, the pulsed increase of P_{CO_2} in the soil subsurface enhanced silicate weathering reactions, demonstrating a direct response of geochemical reactions to ecosystem

changes. The episodic nature of these weathering events emphasizes the overarching control of water availability on the incremental co-evolution of the CZ. Thirdly, dissolution of CO₂ in pore water explains most (60 to 71%) of the deviation of ARQ from the expected soil oxidative ratio. Consumption of dissolved CO₂ in silicate weathering reactions is insufficiently fast to consume this newly dissolved CO₂. Therefore, dissolved CO₂ is transported with water flux to depth and along the soil-bedrock interface, enabling further CO₂ consumption along the water flow paths. Degassing of CO₂ from supersaturated stream water may be an important mechanism that is not reflected in the flux tower measurements if it occurs outside of the statistical measurement footprint of the tower or on a timescale that is not typically captured by NEE partitioning schemes.

The results support a conceptual model where pulsed wetting front propagation initiates a cascade of episodic biogeochemical processes in the soil profile. These reactions are dependent on the initial soil moisture conditions as well as the underlying lithology. Reaction products are capable of propagating into saprolite and along the water flow paths, and of releasing rock dissolution products and CO₂ to the stream. Over long time-scales, these pulsed episodes cumulatively shape the structure and composition of the CZ.

Acknowledgments

All data utilized in this paper are available through the criticalzone.org website at <http://criticalzone.org/catalina-jemez/data/>. This research was funded by the National Science Foundation, grant EAR-1331408, which supports the Catalina-Jemez Critical Zone Observatory, and through the Binational Agricultural Research and Development (BARD) program, which awarded a postdoctoral fellowship to Y. Olshansky (grant FI-534-2015). We are grateful to Mary Kay Amistadi and Rachel Nadine Burnett for assistance with laboratory chemical analyses and field work.

References

- Akima, H., & Gebhardt, A. (2016). akima: Interpolation of Irregularly and Regularly Spaced Data. <https://cran.r-project.org/package=akima>
- Andrews, J. A., & Schlesinger, W. H. (2001). Soil CO₂ dynamics, acidification, and chemical weathering in a temperate forest with experimental CO₂ enrichment. *Global Biogeochemical Cycles*, *15*(1), 149–162. <https://doi.org/10.1029/2000GB001278>
- Angert, A., Yakir, D., Rodeghiero, M., Preisler, Y., Davidson, E. A., & Weiner, T. (2015). Using O₂ to study the relationships between soil CO₂ efflux and soil respiration. *Biogeosciences*, *12*(7), 2089–2099. <https://doi.org/10.5194/bg-12-2089-2015>
- Barron-Gafford, G. A., Scott, R. L., Jenerette, G. D., & Huxman, T. E. (2011). The relative controls of temperature, soil moisture, and plant functional group on soil CO₂ efflux at diel, seasonal, and annual scales. *Journal of Geophysical Research*, *116*, G01023. <https://doi.org/10.1029/2010JG001442>
- Birch, H. F. (1958). The effect of soil drying on humus decomposition and nitrogen availability. *Plant and Soil*, *10*(1), 9–31. <https://doi.org/10.1007/BF01343734>
- Brantley, S. L., & Olsen, A. A. (2013). *Reaction kinetics of primary rock-forming minerals under ambient conditions* (2nd ed.). Amsterdam, Netherlands: Elsevier Ltd.
- Brown-Mitic, C., Shuttleworth, W. J., Chawn Harlow, R., Petti, J., Burke, E., & Bales, R. (2007). Seasonal water dynamics of a sky island subalpine forest in semi-arid southwestern United States. *Journal of Arid Environments*, *69*(2), 237–258. <https://doi.org/10.1016/j.jaridenv.2006.09.005>
- Burba, G. G., McDermitt, D. K., Grelle, A., Anderson, D. J., & Xu, L. (2008). Addressing the influence of instrument surface heat exchange on the measurements of CO₂ flux from open-path gas analyzers. *Global Change Biology*, *14*(8), 1854–1876. <https://doi.org/10.1111/j.1365-2486.2008.01606.x>
- Calabrese, S., Porporato, A., & Parolari, A. J. (2017). Hydrologic transport of dissolved inorganic carbon and its control on chemical weathering. *Journal of Geophysical Research: Earth Surface*, *122*, 2016–2032. <https://doi.org/10.1002/2017JF004346>
- Chadwick, O. A., & Chorover, J. (2001). The chemistry of pedogenic thresholds. *Geoderma*, *100*(3-4), 321–353. [https://doi.org/10.1016/S0016-7061\(01\)00027-1](https://doi.org/10.1016/S0016-7061(01)00027-1)
- Chang, L.-L., Dwivedi, R., Knowles, J. F., Fang, Y.-H., Niu, G.-Y., Pelletier, J. D., et al. (2018). Why do large-scale land surface models produce a low ratio of transpiration to evapotranspiration? *Journal of Geophysical Research: Atmospheres*, *123*, 9109–9130. <https://doi.org/10.1029/2018JD029159>
- Chorover, J., & Amistadi, M. K. (2001). Reaction of forest floor organic matter at goethite, birnessite and smectite surfaces. *Geochimica et Cosmochimica Acta*, *65*(1), 95–109. [https://doi.org/10.1016/S0016-7037\(00\)00511-1](https://doi.org/10.1016/S0016-7037(00)00511-1)
- Chorover, J., Vitousek, P. M., Everson, D. A., Esperanza, A. M., & Turner, D. (1994). Solution chemistry profiles of mixed-conifer forests before and after fire. *Biogeochemistry*, *26*(2), 115–144. <https://doi.org/10.1007/BF02182882>
- Cueva, A., Volkmann, T. H. M., van Haren, J., Troch, P. A., & Meredith, L. K. (2019). Reconciling negative soil CO₂ fluxes: Insights from a large-scale experimental hillslope. *Soil Systems*, *3*(1), 10. <https://doi.org/10.3390/soilsystems3010010>
- Eberl, D. D. (2003). *User guide to RockLock-A program for determining quantitative mineralogy from X-ray diffraction data*. <https://doi.org/10.3133/ofr200378>
- Falge, E., Baldocchi, D., Olson, R., Anthoni, P., Aubinet, M., Bernhofer, C., et al. (2001). Gap filling strategies for defensible annual sums of net ecosystem exchange. *Agricultural and Forest Meteorology*, *107*(1), 43–69. [https://doi.org/10.1016/S0168-1923\(00\)00225-2](https://doi.org/10.1016/S0168-1923(00)00225-2)
- Fiedler, S., Vepraskas, M. J., & Richardson, J. L. (2007). *Soil redox potential: Importance, field measurements, and observations*. *advances in agronomy* (pp. 1–54). San Diego, CA: Elsevier Masson SAS.
- Fox, J., & Weisberg, S. (2011). *An R companion to applied regression* (2nd ed.). Thousand Oaks, CA: Sage.
- Joseph, W.C. (1968). Structural geology of the Mt. Bigelow-Bear Wallow-Mt. Lemmon area, Santa Catalina Mountains, Arizona. <http://hdl.handle.net/10150/565165>
- Lee, X., Massman, W., & Law, B. (2004). *Handbook of micrometeorology: a guide for surface flux measurement and analysis*. Dordrecht: Springer Science & Business Media.
- Lenth, R. (2015). lsmeans: Least-Squares Means. <http://cran.r-project.org/package=lsmeans>
- Leone, J. D., Holbrook, W. S., Chorover, J., & Carr, B. (2016). Effect of metamorphic foliation on regolith thickness, Catalina Critical Zone Observatory, Arizona. AGU Fall Meet. Abstr.: EP43C-0979.
- Li, L., Maher, K., Navarre-Sitchler, A., Druhan, J., Meile, C., Lawrence, C., et al. (2017). Expanding the role of reactive transport models in critical zone processes. *Earth-Science Reviews*, *165*, 280–301. <https://doi.org/10.1016/j.earscirev.2016.09.001>

- Lybrand, R. A., & Rasmussen, C. (2018). Climate, topography, and dust influences on the mineraland geochemical evolution of granitic soils in southern Arizona. *Geoderma*, 314, 245–261. <https://doi.org/10.1016/j.geoderma.2017.10.042>
- Masiello, C. A., Gallagher, M. E., Randerson, J. T., Deco, R. M., & Chadwick, O. A. (2008). Evaluating two experimental approaches for measuring ecosystem carbon oxidation state and oxidative ratio. *Journal of Geophysical Research*, 113, G03010. <https://doi.org/10.1029/2007JG000534>
- McIntosh, J. C., Schaumberg, C., Perdril, J., Harpold, A., Vázquez-Ortega, A., Rasmussen, C., et al. (2017). Geochemical evolution of the critical zone across variable time scales informs concentration-discharge relationships: Jemez River Basin critical zone observatory. *Water Resources Research*, 53, 4169–4196. <https://doi.org/10.1002/2016WR019712>
- Moore, D. M., & Reynolds, R. C. (1997). *X-ray diffraction and the identification and analysis of clay minerals* (2nd ed.). New York: Oxford University Press.
- Oh, N. H., Hofmockel, M., Lavine, M. L., & Richter, D. D. (2007). Did elevated atmospheric CO₂ alter soil mineral weathering?: An analysis of 5-year soil water chemistry data at Duke FACE study. *Global Change Biology*, 13(12), 2626–2641. <https://doi.org/10.1111/j.1365-2486.2007.01452.x>
- Pelletier, J. D., & Rasmussen, C. (2009). Geomorphically based predictive mapping of soil thickness in upland watersheds. *Water Resources Research*, 45, W09417. <https://doi.org/10.1029/2008WR007319>
- Perdril, J., Thompson, A., & Chorover, J. (2015). *Chapter 6 – Soil geochemistry in the critical zone: influence on atmosphere, surface- and groundwater composition*. Amsterdam, Netherlands: Elsevier B.V.
- Pinheiro, J., Bates, D., DebRoy, S., Sarkar, D., & R Core Team. (2017). {nlme}: Linear and nonlinear mixed effects models. <https://cran.r-project.org/package=nlme>
- Placella, S. A., Brodie, E. L., & Firestone, M. K. (2012). Rainfall-induced carbon dioxide pulses result from sequential resuscitation of phylogenetically clustered microbial groups. *Proceedings of the National Academy of Sciences*, 109(27), 10,931–10,936. <https://doi.org/10.1073/pnas.1204306109>
- R Core Team. (2017). R: A language and environment for statistical computing. <https://www.r-project.org/>
- Rasmussen, C., Troch, P. A., Chorover, J., Brooks, P., Pelletier, J., & Huxman, T. E. (2011). An open system framework for integrating critical zone structure and function. *Biogeochemistry*, 102(1-3), 15–29. <https://doi.org/10.1007/s10533-010-9476-8>
- Reichstein, M., Falge, E., Baldocchi, D., Papale, D., Aubinet, M., Berbigier, P., et al. (2005). On the separation of net ecosystem exchange into assimilation and ecosystem respiration: review and improved algorithm. *Global Change Biology*, 11(9), 1424–1439. <https://doi.org/10.1111/j.1365-2486.2005.001002.x>
- Sánchez-Cañete, E. P., Barron-Gafford, G. A., & Chorover, J. (2018). A considerable fraction of soil-respired CO₂ is not emitted directly to the atmosphere. *Scientific Reports*, 8(1), 13518. <https://doi.org/10.1038/s41598-018-29803-x>
- Schoeneberger, P. J., Wysocki, D. A., Benham, E. C., & Soil survey staff (2012). *Field book for describing and sampling soils* (3rd ed.). Lincoln, NE.
- Smith, A. P., Bond-Lamberty, B., Benschoter, B. W., Tfaily, M. M., Hinkle, C. R., Liu, C., & Bailey, V. L. (2017). Shifts in pore connectivity from precipitation versus groundwater rewetting increases soil carbon loss after drought. *Nature Communications*, 8(1), 1335–1311. <https://doi.org/10.1038/s41467-017-01320-x>
- Sposito, G. (1984). *The surface chemistry of soils*. New York: Oxford University Press.
- Stumm, W., & Morgan, J. J. (1996). *Aquatic chemistry: Chemical equilibria and rates in natural waters*. New York Chichester: Wiley.
- Taylor, L. L., Leake, J. R., Quirk, J., Hardy, K., Banwart, S. A., & Beerling, D. J. (2009). Biological weathering and the long-term carbon cycle: Integrating mycorrhizal evolution and function into the current paradigm. *Geobiology*, 7(2), 171–191. <https://doi.org/10.1111/j.1472-4669.2009.00194.x>
- Vázquez-Ortega, A., Perdril, J., Harpold, A., Zapata-Ríos, X., Rasmussen, C., McIntosh, J., et al. (2015). Rare earth elements as reactive tracers of biogeochemical weathering in forested rhyolitic terrain. *Chemical Geology*, 391, 19–32. <https://doi.org/10.1016/j.chemgeo.2014.10.016>
- White, A. F., & Brantley, S. L. (2003). The effect of time on the weathering of silicate minerals: Why do weathering rates differ in the laboratory and field? *Chemical Geology*, 202(3–4), 479–506. <https://doi.org/10.1016/j.chemgeo.2003.03.001>
- Wickham, H. (2009). *ggplot2: Elegant graphics for data analysis*. New York: Springer-Verlag. <https://doi.org/10.1007/978-0-387-98141-3>
- Xiang, S. R., Doyle, A., Holden, P. A., & Schimel, J. P. (2008). Drying and rewetting effects on C and N mineralization and microbial activity in surface and subsurface California grassland soils. *Soil Biology and Biochemistry*, 40(9), 2281–2289. <https://doi.org/10.1016/j.soilbio.2008.05.004>
- Zhang, X., Niu, G.-Y., Elshall, A. S., Ye, M., Barron-Gafford, G. A., & Pavao-Zuckerman, M. (2014). Assessing five evolving microbial enzyme models against field measurements from a semiarid savannah—What are the mechanisms of soil respiration pulses? *Geophysical Research Letters*, 41, 6428–6434. <https://doi.org/10.1002/2014GL061399>

Erratum

In the originally published version of this article, Figure 3 did not include the appropriate legend in the right margin. The figure has since been corrected, and this version may be considered the authoritative version of record.